Rodolfo Marcilli Perissinotto
School of Mechanical Engineering,
University of Campinas,
Rua Mendeleyev, 200,
Cidade Universitária, Campinas,
São Paulo 13083-860, Brazil
e-mail: rodolfomp@fem.unicamp.br

William Monte Verde
Center for Petroleum Studies,
Rua Cora Coralina, 350,
Cidade Universitária, Campinas,
São Paulo 13083-896, Brazil
e-mail: wmv@unicamp.br

Jorge Luiz Biazussi
Center for Petroleum Studies,
Rua Cora Coralina, 350,
Cidade Universitária, Campinas,
São Paulo 13083-896, Brazil
e-mail: biazussi@unicamp.br

Marcelo Souza de Castro
School of Mechanical Engineering,
University of Campinas,
Rua Mendeleyev, 200,
Cidade Universitária, Campinas,
São Paulo 13083-860, Brazil
e-mail: mcastro@fem.unicamp.br

Antonio Carlos Bannwart
School of Mechanical Engineering,
University of Campinas,
Rua Mendeleyev, 200,
Cidade Universitária, Campinas,
São Paulo 13083-860, Brazil
e-mail: bannwart@fem.unicamp.br

Experimental Analysis on the Velocity of Oil Drops in Oil–Water Two-Phase Flows in Electrical Submersible Pump Impellers

The objective of this research is to investigate the velocity of oil drops within the impeller of an electrical submersible pump (ESP) working with oil-in-water dispersion flows at different operational conditions. An experimental study was conducted using an ESP prototype with a transparent shell designed to enable flow visualization within the impeller channels. The tests were performed at three rotational speeds, 600, 900, and 1200 rpm, for three water flow rates, 80%, 100%, and 120% of the best efficiency point (BEP). A high-speed camera (HSC) with a lighting set captured images of the oil-in-water dispersion at 1000 frames per second. The images observation suggests the presence of a turbulent flow in the impeller. The turbulence, associated with high rotation Reynolds numbers, causes the oil drops to become smaller as the impeller rotational speed and the water flow rate increase. Despite this rotating environment, the oil drops generally have a spherical shape. Regarding the kinematics, the images processing reveals that the velocity of oil drops has a magnitude around a unit of m/s. The velocity depends on the oil drop position in the channel: oil drops that stay close to a suction blade (SB) have significantly higher velocities than oil drops that stay close to a pressure blade (PB). Considering a complex flow with water velocity profiles and pressure gradients, the analysis of oil velocity curves indicates the occurrence of accelerations that may be caused by drag and pressure forces acting on the oil drops. [DOI: 10.1115/1.4042000]

1 Introduction

The electrical submersible pump (ESP) is one of the most important artificial lift devices used in oil production. The ESP consists of a multistage centrifugal pump that provides energy to the petroleum to lift it to the production facilities. There are more than 150,000 wells operating with ESPs worldwide [1].

The ESP usually works with multiphase flows, in the presence of oil, water, and gas. Unfortunately, the presence of water may increase the oil effective viscosity. Therefore, the operation with oil–water flows affects the pump behavior and causes performance losses, leading to significant rises in operational costs.

In applications with heavy oil and high water fractions, for example, the phase distribution can be arranged as a dispersion. The formation of dispersions and emulsions is common in ESP's impellers, since the rotating environment promotes the breaking of the phases into small drops. The ESP impeller may also influence the emulsion stability, which is a function of fluid properties but also of the amount of energy dissipated in the liquid–liquid flow [2].

Understanding the flow within impellers is crucial to build a set of assumptions regarding the formation of high viscosity dispersions and emulsions. As the phase arrangement may impact the ESP behavior, the comprehension of multiphase flow dynamics is essential to design new efficient and longer lasting ESPs.

Considerable efforts have been made to improve the phenomenological understanding of multiphase flows in centrifugal pumps, especially in the case of two-phase gas–liquid flows. Initial studies focused on the nuclear industry, where pumps were employed in reactor cooling systems. In the petroleum industry, Estevam [3] was the first author to develop a pump prototype with a transparent shell for experimental visualization of air bubbles.

Barrios and Prado [4], Trevisan and Prado [5], Zhang et al. [6], Monte Verde et al. [7], and Cubas Cubas [8] are examples of studies in which experimental facilities were designed and built to investigate flow patterns and analyze the behavior of gas bubbles within pump impellers. The authors used high-speed cameras (HSC) to visualize the flow. High-speed imaging is actually a powerful method that enables the observation of fast transient phenomena with high spatial and temporal resolutions [9].

Minemura and Murakami [10] theoretically studied the dynamics of small air bubbles in impellers. The authors concluded that three forces chiefly govern the motion of a bubble in an impeller: the drag force due to the motion of the bubble relative to water, the force caused by pressure gradients in the flow field, and the force due to a virtual mass of the liquid medium. Other forces acting on a bubble as inertia, buoyancy, and hysteresis are negligibly small in the case of air. According to the authors, air bubbles and water on the suction side of the impeller blades move faster than those on the pressure side. The air bubbles move slower than

Contributed by the Ocean, Offshore, and Arctic Engineering Division of ASME for publication in the Journal of Offshore Mechanics and Arctic Engineering. Manuscript received September 5, 2017; final manuscript received November 6, 2018; published online January 17, 2019. Assoc. Editor: Longfei Xiao.

water in the impeller, and larger bubbles have higher velocities relative to water.

Sabino [11] experimentally studied the air bubble dynamics in a centrifugal pump. The author visualized a population of bubbles and identified three typical trajectories: bubbles that move next to the suction blade (SB) without suffering lateral deviations, bubbles that enter the channel near the suction blade but deviate toward the impeller center, and bubbles that enter the channel near the suction blade but deviate toward the pressure blade (PB). The author also calculated the velocity of bubbles as a function of their position. The results revealed that bubbles next to the suction blade move faster than bubbles far from it. Higher rotational speeds result in faster bubbles, but the water flow rate and bubble diameter do not influence the velocity of the fluid particles.

Although there are many papers on gas–liquid flows, there are only a few studies available in the literature concerning two-phase liquid–liquid flows in pumps. Khalil et al. [12], Morales et al. [13], and Bulgarelli et al. [14] are examples of authors who conducted experimental researches on dispersions in centrifugal pumps.

Khalil et al. [12] studied the pump performance behavior with oil-in-water emulsions. They concluded that the presence of emulsions degrades the head and efficiency, especially when the holdup and temperature decrease.

Morales et al. [13] studied the formation of dispersions in a pump. They measured the size distribution of liquid drops and concluded that their characteristic size decreases as the impeller rotational speed increases.

Bulgarelli et al. [14] studied the phase inversion phenomena inside an ESP with eight stages. They observed that the phase inversion occurs at water fractions between 10% and 30%. With a low water fraction, oil is the continuous phase and the high effective viscosity impairs the ESP performance. On the other hand, when the water fraction is sufficiently high, water becomes the continuous phase, the viscosity decreases, and the ESP works normally.

In conclusion, some studies in the literature investigate the motion of gas bubbles in impellers, while others analyze the performance of ESPs with dispersions and emulsions. However, there is a lack of studies on visualization and dynamics of liquid drops, despite the importance of this subject to the industry.

In this paper, based on Perissinotto et al. [15], an experimental study is conducted with focus on flow visualization in order to investigate the behavior of oil drops in a water flow within an ESP impeller. This study aims to analyze the size, shape, trajectory, and velocity of oil drops in different flow conditions. The main objective is to provide a better comprehension on the motion of the dispersed phase. The oil trajectory may reveal the water pathlines, as the oil drops are being carried by water in the channels. Smaller drops may also serve as tracers to indicate the water velocity profiles.

The results achieved in this paper may contribute to validate computational fluid dynamics simulations and may also complement theoretical studies. In the future, the determination of water velocities may enable the estimation of the slip between the liquid phases, considering the drift flux model. Based on this model, the industrial application of this work is to help the development of a one-dimensional model that will represent the performance of ESPs for use in the petroleum industry. The intention is to predict the best type of pump for each application as well as to suggest geometric modifications that may improve the efficiency of new pumps.

2 Experimental Description

Performance and visualization experiments were conducted using an ESP prototype and a HSC. This section describes the experimental facility, characterizes the fluids properties and discusses the test matrix.

Fig. 1 Electrical submersible pump prototype with transparent shell for flow visualization

2.1 Experimental Facility. The main component of the experimental facility is an ESP prototype designed to allow the flow visualization in the impeller. As can be seen in Fig. 1, the prototype has a transparent top shroud made of an acrylic material, which enables the visualization of all the channels simultaneously. The prototype was developed, built, and used by Monte Verde et al. [7] with two-phase gas–liquid flows. It was then adapted to perform tests with two-phase liquid–liquid mixtures.

The experimental loop consists of the ESP prototype, a water flow line, and an oil injection system. The water circuit has a separation tank, a booster pump, and a water flow meter. The oil system is composed of a peristaltic pump, an oil reservoir, and stainless steel capillary tubes. A photograph of the complete facility is shown in Fig. 2.

In the water line, the booster pump draws water from the separation tank. The water flows through the pipelines and reaches the prototype suction. At the same time, in the oil system, the peristaltic pump drags oil out of the reservoir. The oil is injected into the prototype, in a point next to the impeller inlet. Thus, the oil becomes dispersed in the water flow. The dispersion enters the impeller, while a high-speed camera captures images of the flow.

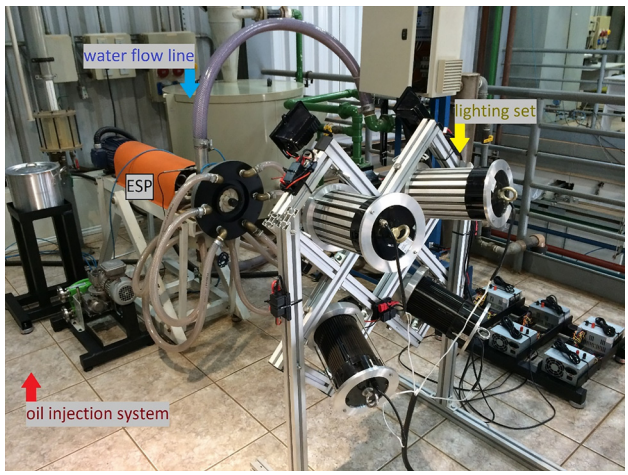

Fig. 2 Experimental facility with ESP prototype, water circuit, and oil system

Table 1 Main features of the measuring instruments

Instrument	Brand/model	Range	Uncertainty
Flow meter	Emerson Micro Motion F100	0–32,650 kg/h	±0.2%
Thermocouple	PT 100 RTD	0–100 °C	±0.5%
Pressure transducers	Emerson Rosemount 2088	0–2000 kPa	±0.075%
Tachometer	Minipa MDT 2238A	2.4–99,999 rpm	—

The mixture then leaves the impeller and finally flows back to the separation tank, where the fluids are gravitationally separated.

A Coriolis flow meter measures the water flow rate (Q), a thermocouple quantifies the mixture temperature, and two capacitive pressure transducers measure the pressures at prototype inlet (P_1) and outlet (P_2). All the signals from the instrumentation are acquired, monitored, and processed in a computer with a software designed in LabVIEW platform. The prototype rotational speed (N) is obtained manually, using a tachometer. Control valves regulate flow rates and pressure levels. In addition, a variable speed driver controls the rotational speed of each pump (water and oil). The technical features of the instruments are detailed in Table 1.

2.2 Experimental Matrix. Performance experiments were conducted with water single-phase flow. Then, performance and visualization experiments were conducted with oil-in-water flow. In this case, tap water and mineral oil were employed.

Chemical tests were performed to characterize the oil properties at 25 °C and yielded a density of 880 kg/m^3, a dynamic viscosity of 220 cP and an interfacial tension with water of 34 mN/m.

The transparent oil was darkened with a black dye to enhance the contrast between the liquids and consequently to improve the quality of the flow images. The dye does not affect the oil properties.

Flow images were captured by a camera IDT (Pasadena, CA) MOTION PRO X with a resolution of 1024 × 1024 pixels at an acquisition rate of 1000 frames per second, and a lens Nikon (Tokyo, Japan) Micro-Nikkor® f/2.8 with a focal length of 60 mm. light-emitting diode reflector luminaires were used as light sources.

The visualization tests were carried out at nine operational conditions, as Table 2 exposes. Three rotational speeds (N) and three water flow rates (Q) around the best efficiency point (BEP) were selected. The oil was injected at a constant flow rate of 2 ml/s (0.122 in^3/s). The water flow rates corresponding to the BEP (Q_{BEP}) were defined by Monte Verde et al. [7] and then confirmed by the performance experiments results.

The chosen rotational speeds are quite lower than those normally used in typical applications of ESPs, which reach 3500 rpm. The selection of rotations from 600 rpm to 1200 rpm was due to limitations of the visualization equipment. At higher rotational speeds, the oil drops become so small and fast that the camera temporal and spatial resolutions are insufficient to generate satisfactory images.

3 Experimental Results

The results are divided into four sections. The ESP performance curves are presented in Sec. 3.1. Some images of the oil-in-water flow are presented in Sec. 3.2 with analysis of the main characteristics of oil drops. Then, a detailed study of velocities of oil drops with different trajectories is presented in Sec. 3.3, in addition to physical interpretations. A brief introduction of drop dynamics is finally performed in Sec. 3.4.

Table 2 Matrix of visualization experiments with oil-in-water dispersion

N (rpm)	$Q = 0.8\ Q_{BEP}$ (m^3/h)	$Q = 1.0\ Q_{BEP}$ (m^3/h)	$Q = 1.2\ Q_{BEP}$ (m^3/h)
600	1.70	2.13	2.56
900	2.56	3.20	3.84
1200	3.40	4.26	5.11

3.1 Pump Performance With Single-Phase and Two-Phase Flows. Experiments were carried out without oil injection to determine performance curves of the ESP prototype operating with water single-phase flow. The results are available in Fig. 3, which shows the pressure increments ($P_2 - P_1$) as a function of the water flow rates (Q) at each rotational speed (N). As can be observed, the prototype performance curves obtained experimentally are in accordance with the results of Monte Verde et al. [7].

The experiments were then repeated with presence of oil. The pump performance with the oil-in-water dispersion was practically identical to the single-phase flow results, with deviations lower than 2%. Therefore, the injection of 2 ml/s (0.122 in^3/s) of oil does not cause performance losses to the ESP. This oil flow rate actually represents less than 1% when compared with the water flow rates at BEP.

3.2 Qualitative Analysis of Flow Images. The visualization experiments resulted in thousands of images, which reveal the occurrence of dispersed oil drops in a continuous water flow pattern in the impeller. All the oil drops have equivalent diameters between 0.1 mm and 5.0 mm (0.20 in).

The oil drops become smaller when the rotational speed increases, as Figs. 4, 5, and 6 expose, for 600 rpm, 900 rpm, and 1200 rpm, respectively. The water flow rates were set at BEP for each rotation, according to Table 2.

The same behavior is noticed with the water flow rate. The oil drops become smaller when the water flow rate increases, as Figs. 7–9 illustrate, for 80%, 100%, and 120% of the BEP, at a constant rotational speed of 900 rpm.

This reduction in the characteristic sizes can be explained by the flow conditions. Higher rotational speeds and flow rates imply more turbulence with velocity gradients and centrifugal forces. This condition is associated with high local shear stress and high kinetic energy, which act on the oil drop breakage [16] inside the pump and within the impeller channels. The rotation Reynolds number (Re_ω) suggests the occurrence of turbulent flows in the impeller. This number compares inertial forces with viscous forces. In the case of our oil-in-water dispersion, Re_ω is a function

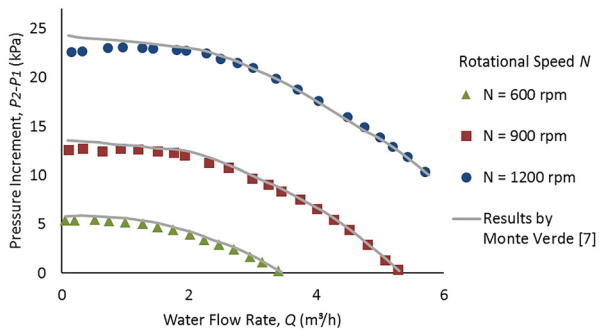

Fig. 3 Performance curves for ESP prototype working with water single-phase flow

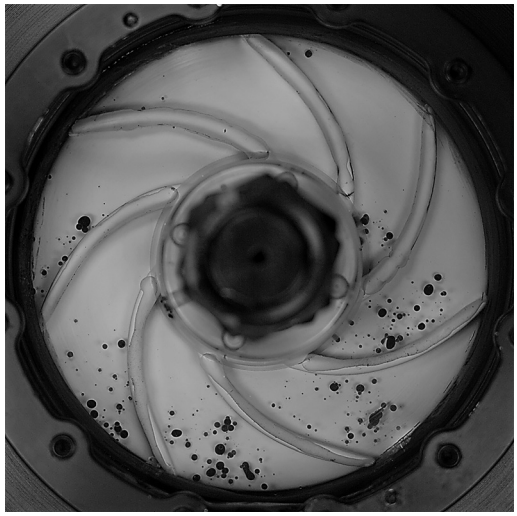

Fig. 4 Image of impeller at 600 rpm and water flow rate at best efficiency point. The impeller rotates clockwise.

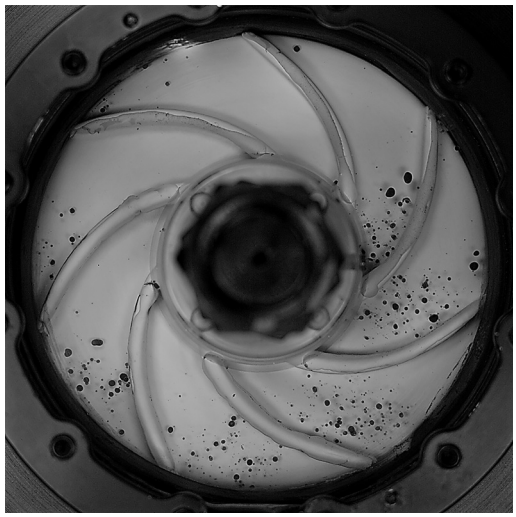

Fig. 5 Image of impeller at 900 rpm and water flow rate at best efficiency point. The impeller rotates clockwise.

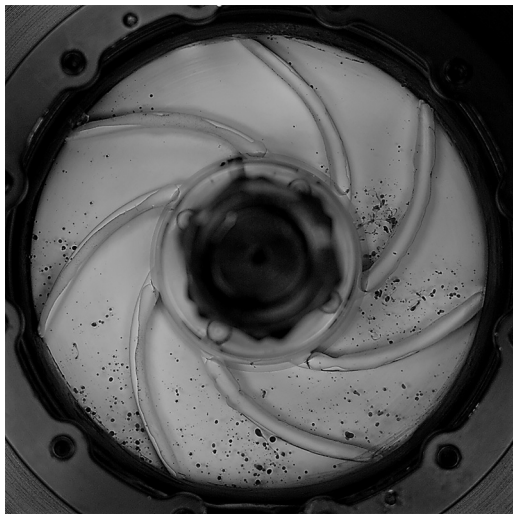

Fig. 6 Image of impeller at 1200 rpm and water flow rate at best efficiency point. The impeller rotates clockwise.

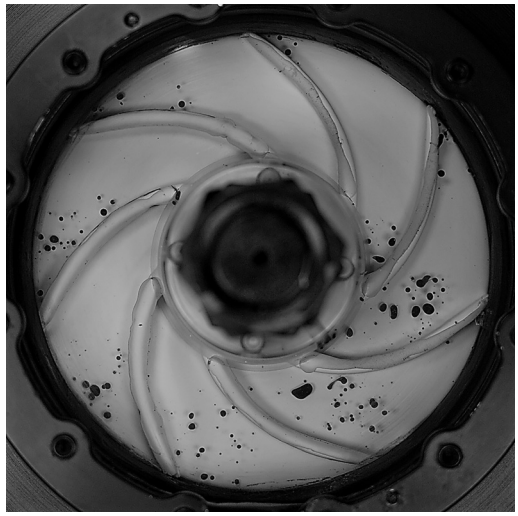

Fig. 7 Image of impeller at 900 rpm and 80% of Q_{BEP}. Impeller rotates clockwise.

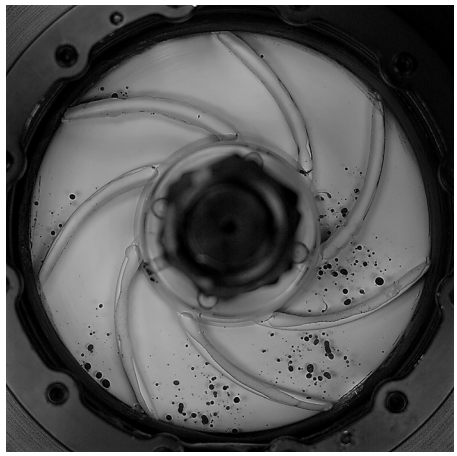

Fig. 8 Image of impeller at 900 rpm and 100% of Q_{BEP}. Impeller rotates clockwise.

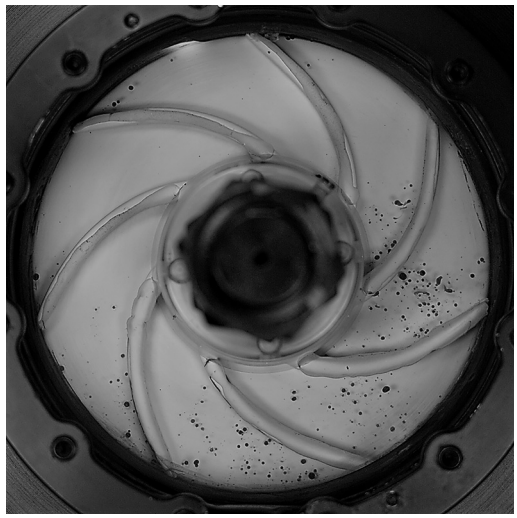

Fig. 9 Image of impeller at 900 rpm and 120% of Q_{BEP}. Impeller rotates clockwise.

of the density (ρ) and viscosity (μ) of water, and the angular speed (ω) and diameter (D) of the impeller

$$\mathrm{Re}_\omega = \frac{\rho \omega D^2}{\mu} \tag{1}$$

The rotation Reynolds number reaches $\mathrm{Re}_\omega = 1.5 \times 10^6$ at $N = 1200$ rpm. There is no consensus on the critical number that determines the transition from laminar to turbulent regime in impellers. However, the images and the high Re_ω strongly indicate the presence of a turbulent water flow, where the oil drops are dispersed and thus exhibit a chaotic motion.

Despite the breakage events, the small oil drops generally tend to remain in a spherical shape, especially from the middle to the impeller outlet. This fact may be explained by the Eötvös or Bond number (Eo). This number is a measure of the importance of body force compared to surface tension force for fluid particles in infinite media [16]. In the case of our oil-in-water dispersion, Eo depends on gravity (g), the difference between the water and oil densities ($\Delta\rho$), the equivalent spherical diameter of the oil drop (d), and the interfacial tension between water and oil (σ)

$$\mathrm{Eo} = \frac{\Delta \rho g d^2}{\sigma} \tag{2}$$

A small oil drop with $d = 1.0$ mm has $\mathrm{Eo} = 0.034$. Hence, the surface tension forces are almost 30 times higher than the body forces, and the oil drop tends to remain spherical, without deformations. On the other hand, a large oil drop with $d = 5.0$ mm has $\mathrm{Eo} = 0.85$. Thus, both forces have the same order of magnitude, and the oil drop may deform and break up. Although the Eötvös or Bond number does not consider the impeller rotating environment, it gives some useful information to the comprehension of the qualitative observations.

3.3 Evaluation of Oil Drop Velocity. The images captured at 600 rpm and BEP were processed to enable the determination of positon and velocity of oil drops.

A LabVIEW routine was developed to remove the rotation from the impeller. The result is a stationary impeller in the processed images. The rotation removal is crucial to the analysis of the oil drops trajectories.

Then, the software IDT MOTION STUDIO was used to track a population of drops. Velocities were finally calculated by identifying differences between the oil drops positions in consecutive images.

The position as a function of time was determined in a Cartesian coordinate system with origin at the impeller's center. With the x and y position of each drop, a polar coordinate system was used to calculate the radial velocity, V_R, and the tangential velocity, V_T. The velocities are obtained with numerical derivatives of the oil drop position r and θ in time t. The time interval Δt is defined by the HSC. In the visualization experiments, an acquisition rate of 1000 fps was used, thus $\Delta t = 0.001$s

$$V_R = \Delta r / \Delta t \tag{3}$$

$$V_T = r(\Delta \theta / \Delta t) \tag{4}$$

The radial and angular position, r and θ, are related to the position x and y

$$r = \sqrt{x^2 + y^2} \tag{5}$$

$$\theta = \tan^{-1}(y/x) \tag{6}$$

In total, 75 drops were analyzed. The majority presented random trajectories. However, patterns could be identified in 24 oil drops, divided into three cases: oil drops that stay next to a suction blade from inlet to outlet (Fig. 10), oil drops that stay next to a pressure blade from inlet to outlet (Fig. 11), and central oil drops that start the trajectory near a suction blade and end it near a pressure blade (Fig. 12). As the impeller rotates clockwise, the suction blade is on the right and the pressure blade is on the left side of the channel, as indicated in the images.

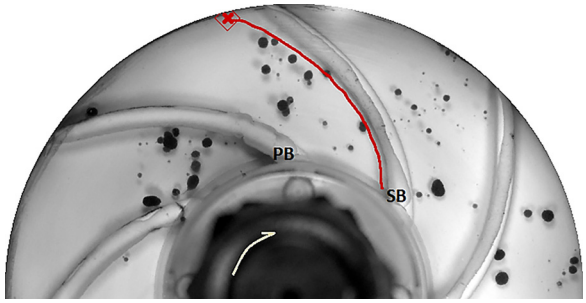

Fig. 10 Example of oil drop with a trajectory close to a SB

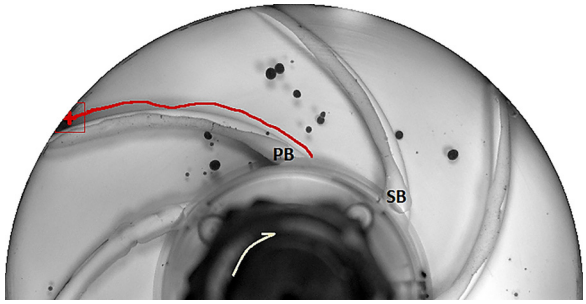

Fig. 11 Example of oil drop with a trajectory close to a PB

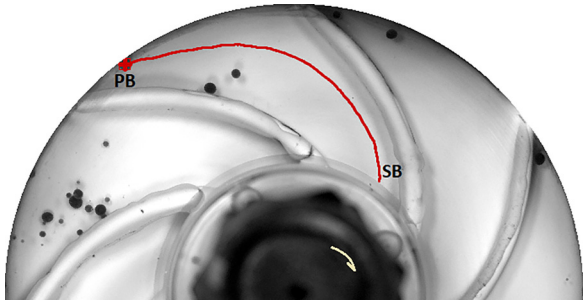

Fig. 12 Example of oil drop with central path, from suction blade to pressure blade

The drops with well-behaved trajectories (with one of the patterns described) had their velocities further analyzed. Sections 3.3.1–3.3.4 present and discuss graphs of velocities V_R and V_T as functions of the radial position r in the flow condition corresponding to $N = 600$ rpm and $Q = Q_{\mathrm{BEP}}$. The radial position varies between 25 mm (0.98 in, internal radius, channel input) and 55 mm (2.16 in, external radius, channel output), approximately.

The choice of evaluating the velocity of oil drops with predictable trajectories aims to facilitate the interpretation of the results. Each graph presented in Secs. 3.3.1–3.3.4 displays velocity curves of oil drops with the same trajectory and at the same flow condition. Thus, the only difference between the curves in a graph is the equivalent diameter of the analyzed oil drops.

The fact that the oil drops perform random trajectories suggests that the water flow in the impeller is full of turbulent phenomena such as jets and vortices, as well as forces acting on both fluids, which lead the mixture to laterally deviate in the channels. This

condition does not invalidate the velocity results nor their use in the industry. The development of models based on the drift-flux model considers the relative velocity between water and oil, regardless of the random nature of their motion.

3.3.1 Central Oil Drops. Twelve drops executed the central trajectory beginning on the suction blade and ending on the pressure blade. Their equivalent diameters (d) range from 1.00 mm (0.039 in) to 3.11 mm (0.122 in). Velocity curves are shown in Figs. 13 and 14.

As can be observed, both velocity components have magnitudes around a unit of meter per second. The velocity V_R undergoes a pronounced reduction as the oil drops move through the channel. The velocity V_T also presents an intense reduction followed by a slight increase near the channel outlet.

Considering the geometry of the channel, similar to a divergent nozzle [17], it is expected that the fluids experience a gradual reduction in their velocities as they flow from entrance to exit. However, it is known that the flow in impellers is also subjected to rotation, with velocity profiles and pressure gradients [18]. In this sense, the central oil drops possibly undergo a gradual increase in pressure while they are moving in the channel. This adverse pressure gradient causes the dispersion to decelerate and deviate from suction to pressure blade.

3.3.2 Oil Drops Next to Suction Blade. Five oil drops performed the trajectory close to the suction blade. Their equivalent diameters (d) range from 0.78 mm (0.031 in) to 3.00 mm (0.118 in). The radial and tangential velocities are displayed in Figs. 15 and 16.

A fourth-order polynomial was fitted with values extracted from the five velocity curves. The result is an average velocity curve, as shown in Figs. 17 and 18. The fourth-order polynomial

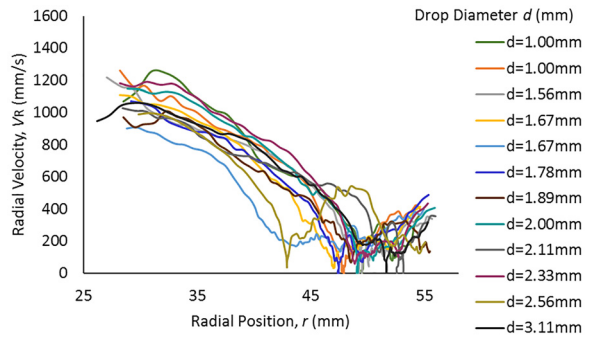

Fig. 13 Radial velocity of 12 central oil drops with different diameters

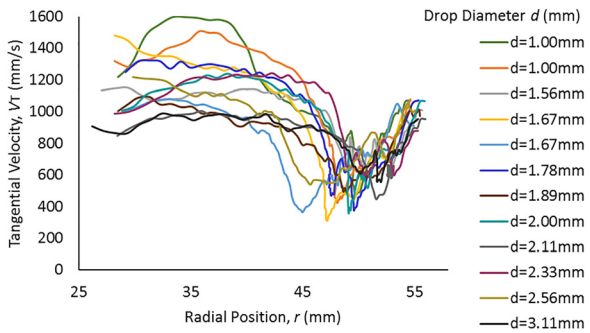

Fig. 14 Tangential velocity of 12 central oil drops with different diameters

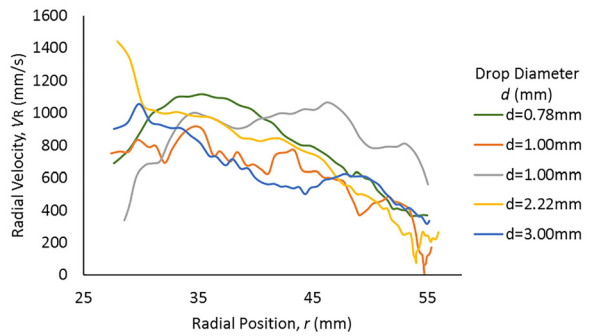

Fig. 15 Radial velocity of five drops with different diameter on suction blade zone

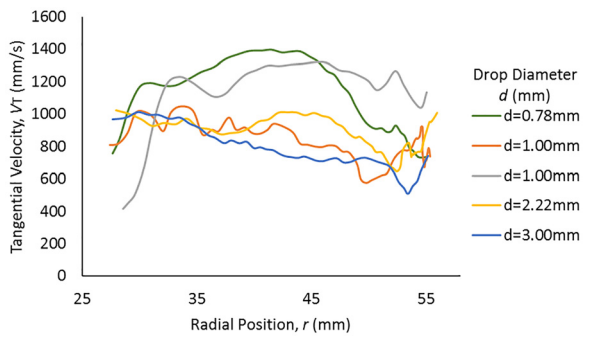

Fig. 16 Tangential velocity of five drops with different diameter on suction blade zone

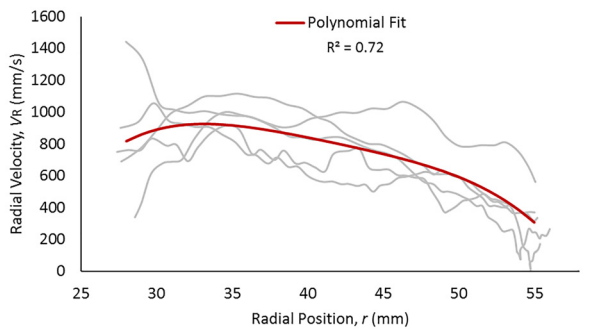

Fig. 17 Average radial velocity of oil drops on the suction blade region

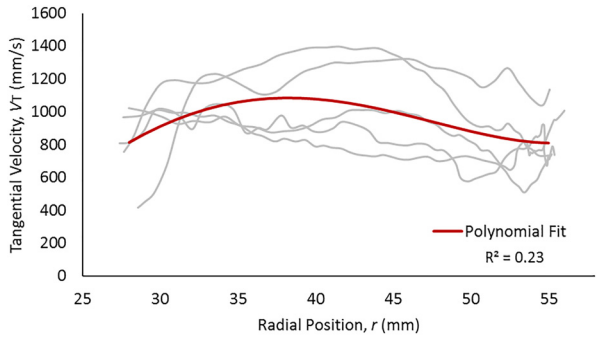

Fig. 18 Average tangential velocity of oil drops on the suction blade region

has the best goodness of fit among the most usual fitting functions.

As can be noticed, both components V_R and V_T suffer a slight increase followed by a small subsequent fall as the drops move in the channel. The average velocity curves fluctuate from 0.3 m/s (1.0 ft/s) to 1.1 m/s (3.6 ft/s) approximately.

3.3.3 Oil Drops Next to Pressure Blade. Seven oil drops presented the trajectory close to the pressure blade. Their equivalent diameters (d) vary from 1.11 mm (0.044 in) to 3.11 mm (0.122 in). Velocities can be seen in Figs. 19 and 20.

A fourth-order polynomial was fitted with values extracted from the seven velocity curves. The result, an average velocity curve, is exposed in Figs. 21 and 22. The fourth-order polynomial has the best goodness of fit among the most usual fitting functions.

As can be observed, both components V_R and V_T undergo a reduction from the beginning to the middle, followed by a growth from the middle to the end of the channel. The magnitudes vary between 0.2 m/s (0.66 ft/s) and 1.0 m/s (3.3 ft/s).

3.3.4 Comparison Between Peripheral Trajectories. The average velocity curves were plotted together in Figs. 23 and 24. The graphs clearly reveal that oil drops on the suction region move with higher velocities than oil drops on the pressure region. The results agree with the conclusions of Minemura and Murakami [10] and Sabino [11] for air bubbles.

The velocity analysis also indicates that the oil drops present very different behaviors depending on their positions in the channel. A drop on the suction blade tends to maintain its velocity or decelerate near the end of its trajectory. On the other hand, a drop on the pressure blade undergoes an intense deceleration at the

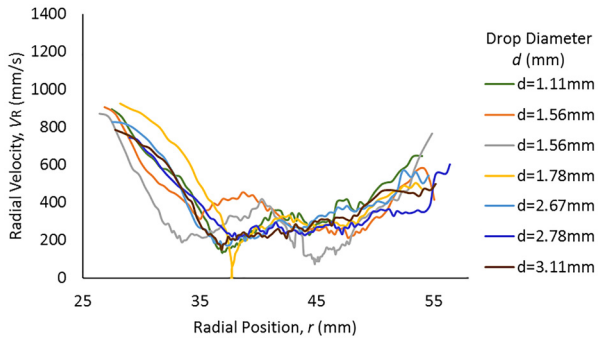

Fig. 19 Radial velocity of seven drops on pressure blade region

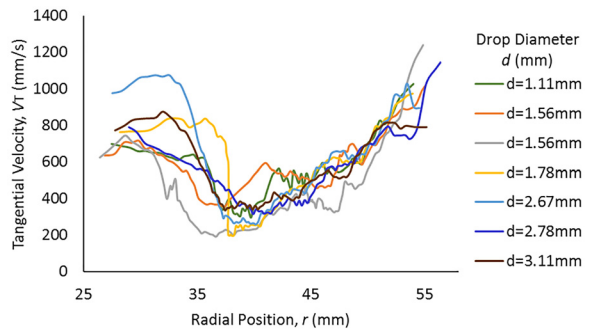

Fig. 20 Tangential velocity of seven drops on pressure blade region

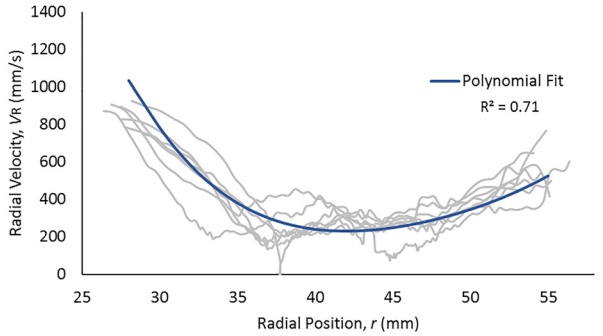

Fig. 21 Average radial velocity of oil drops on the pressure blade region

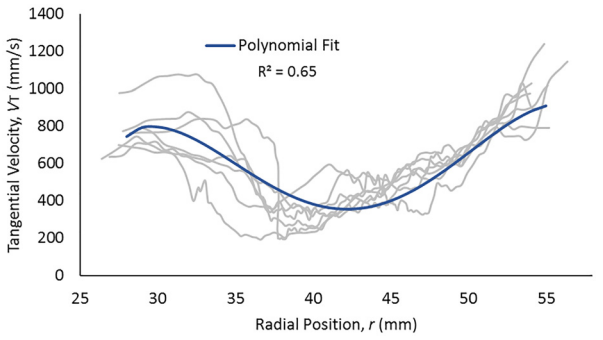

Fig. 22 Average tangential velocity of oil drops on the pressure blade region

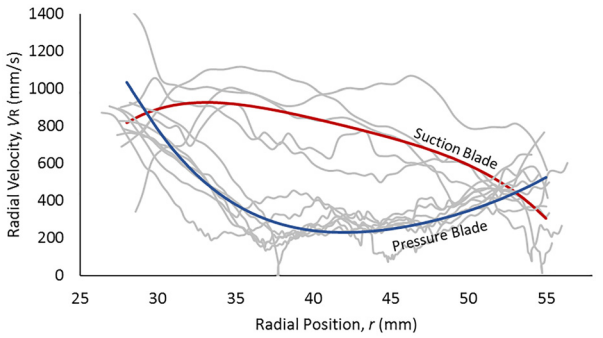

Fig. 23 Comparison between average radial velocities of oil drops on suction blade and on pressure blade

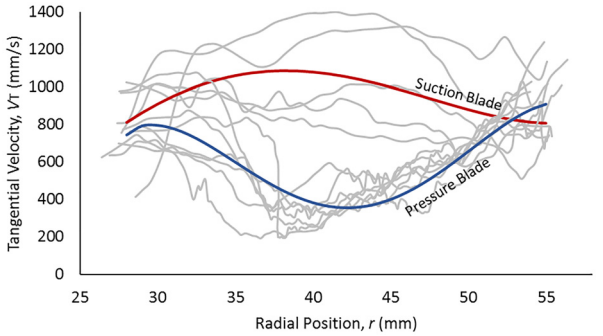

Fig. 24 Comparison between average tangential velocities of oil drops on suction blade and on pressure blade

beginning of its trajectory, followed by a later acceleration near the end.

The differences observed in the velocity curves of Figs. 23 and 24 can be explained by the velocity profiles that regularly occur in single-phase flows within impellers [18]. As the dispersed phase causes insignificant disturbances in the continuous phase flow (Sec. 3.1), the velocities of oil drops may adequately describe the velocity field of the continuous water. Such velocities are strongly coupled since the continuous phase carries the dispersed phase.

Velocity profiles related to one-phase flows in impellers were investigated by some authors, such as Pedersen et al. [19] and Byskov et al. [20]. The authors studied the velocity profiles for water flows at BEP and concluded that the velocities change along the channel, both radially and tangentially. There is an excellent agreement between their results with water and the results achieved in this paper with oil drops.

In the suction blade zone, approximately from the middle to the outlet, the authors observed that the intensity of the velocity vectors decreases along the radius. Thus, a fluid particle in this region would experience a reduction in its velocity, i.e., a situation similar to that observed for the five oil drops in Sec. 3.3.2. On the other hand, in the pressure blade zone, the authors observed that the intensity of the velocity vectors increases along the radius. Therefore, a fluid particle in this region would undergo an increment in its velocity as well, a situation similar to that observed for the seven oil drops in Sec. 3.3.3.

Despite this gradual increase in water velocities in the pressure blade region, velocities related to the suction blade zone tend to be much more intense, in all the channel radial positions. This observation also agrees with the results achieved in Secs. 3.3.2 and 3.3.3 for the 12 oil drops with peripheral trajectories.

3.4 Introduction to Oil Drop Dynamics. As Minemura and Murakami [10] explain, the drag and pressure forces mainly govern the motion of fluid particles. The accelerations and decelerations observed in the velocity curves in Sec. 3.3 are the result of the balance between both forces.

The drag force occurs due to the slip between the phases. Considering the water velocity higher than the oil velocity, the drag force tends to carry the drops out of the impeller. The pressure force, on the other hand, occurs due to the pressure gradient in the channel, which acts contrarily to the movement of the drops. Thus, the pressure force tends to carry the drops back into the impeller inlet.

Considering spherical drops, the drag force $\mathbf{F_d}$ is a function of the water density (ρ), the drop diameter (d), the drag coefficient (C_d), the drop velocity ($\mathbf{V}$), and the water velocity ($\mathbf{W}$)

$$|\mathbf{F_d}| = \frac{1}{2}\rho C_d \left(\frac{\pi d^2}{4}\right)(\mathbf{V}-\mathbf{W})^2 \tag{7}$$

The pressure force ($\mathbf{F_p}$) depends on the drop diameter (d) and the pressure gradient (∇p) along a streamline. The pressure gradient usually includes the effects of centrifugal and Coriolis forces, typical in rotating systems [10]

$$|\mathbf{F_p}| = \left(\frac{\pi d^3}{6}\right)\nabla p \tag{8}$$

The velocity $\mathbf{V}$ that appears in Eq. (7) can be calculated as the vector sum of its radial and tangential components, V_R and V_T, evaluated in Sec. 3.3. However, as the velocity $\mathbf{W}$ and the pressure gradient ∇p are both unknown, the determination of $\mathbf{F_d}$ and $\mathbf{F_p}$ is impossible, unfortunately.

As a suggestion for a future experimental study, the water flow in the prototype impeller could be further investigated with particle image velocimetry equipment. The results would allow the evaluation of forces acting on the oil-in-water dispersion and, therefore, the dynamics of oil drops would be better understood. In fact, calculating $\mathbf{W}$ is a necessary task to the evaluation of the slip between the liquid phases. This information is essential to achieve the development of new models based on the drift-flux model for use in the petroleum industry.

4 Conclusions

This paper investigated the shape, size, trajectory, and velocity of oil drops dispersed in water within an ESP impeller. Experiments were performed with an ESP prototype under different operational conditions. Flow images were captured with a high-speed camera, analyzed, and processed in a computational environment.

The images revealed an inverse dependence between the oil drop characteristic size and the ESP operational conditions, such as impeller rotational speed and water flow rate. Higher rotations and flow rates increase the turbulence in the impeller. This turbulent flow condition facilitates the oil drop breakage.

Although the oil drops undergo deformation and breaking events, the oil drop surface generally appears with a spherical shape in the impeller images. This geometry is a consequence of relatively large surface tension forces when compared with body forces, a condition mainly related to the smaller drops.

Concerning the oil drops motion, 75 drops were studied with processed images. Twelve oil drops executed a central path, five drops remained near a suction blade, and seven drops remained near a pressure blade during their trajectories. The other oil drops presented random trajectories and did not have their velocities compared.

The analysis of kinematics indicates that the oil drops present very different velocities depending on their positions in the channel. Central oil drops decelerate during their trajectories. Drops next to a suction blade accelerate and then decelerate. Drops next to a pressure blade have the inverse behavior.

The velocity of oil drops presents a magnitude around a unit of m/s. However, oil drops on the suction blade region present quite larger velocities than those on the pressure blade region. This result fully agrees with other studies available in the literature, whether with focus on water or with focus on gas bubbles.

The flow within impellers is characterized by complex velocity profiles and pressure gradients. As the oil drops are subjected to such phenomena, fluctuations in their velocities are fully expected. The oil drops motion is mainly defined by the sum of two forces, the drag force, and the pressure force, which depend on relative velocities and pressure gradients along streamlines. Future studies on these topics are strongly recommended in order to complement the results achieved in this paper.

Acknowledgment

The authors thank Equinor Brazil, ANP, and PRH/ANP ("Compromisso de Investimentos com Pesquisa e Desenvolvimento") for providing financial support for this work. Acknowledgments are also extended to CEPETRO/UNICAMP and ALFA—Artificial Lift and Flow Assurance Research Group.

Funding Data

- Equinor Brazil and National Agency of Petroleum, Natural Gas and Biofuels (ANP) provided financial support for this work.

Nomenclature

C_d = drag coefficient
d = equivalent diameter of an oil drop (m)
D = impeller diameter (m)
Eo = Eötvös or bond number
$\mathbf{F_d}$ = drag force (N)
$\mathbf{F_p}$ = pressure force (N)
g = gravity (m/s^2)

N = impeller rotational speed (Hz)
P_1, P_2 = pressures at prototype inlet and outlet (Pa)
Q = water flow rate (m^3/s)
Q_{BEP} = water flow rate at the best efficiency point BEP (m^3/s)
r = radial position of oil drop in a polar system (m)
Re_ω = rotation Reynolds number
$\mathbf{V}$ = velocity vector of an oil drop (m/s)
V_R = radial velocity of an oil drop (m/s)
V_T = tangential velocity of an oil drop (m/s)
$\mathbf{W}$ = velocity vector of water (m/s)
x, y = position of oil drop in a Cartesian system (m)
$\Delta\rho$ = difference of densities (kg/m^3)
Δt = time interval between consecutive images (s)
θ = angular position of oil drop in a polar system
μ = water dynamic viscosity (Pa·s)
ρ = water density (kg/m^3)
σ = surface tension (N/m)
ω = impeller angular speed (rad/s)
∇p = pressure gradient (Pa/m)

References

[1] Flatern, R. V., 2015, "The Defining Series—Electrical Submersible Pumps," Oilfield Rev., **27**(2), pp. 1–2.
[2] Sjoblom, J., 2005, *Emulsions and Emulsion Stability: Surfactant Science Series*, 2nd ed., CRC Press, Boca Raton, FL.
[3] Estevam, V., 2002, "A Phenomenological Analysis About Centrifugal Pump in Two-Phase Flow Operation," Ph.D. thesis, University of Campinas, Campinas, Brazil.
[4] Barrios, L., and Prado, M. G., 2011, "Experimental Visualization of Two-Phase Flow Inside an Electrical Submersible Pump Stage," ASME J. Energy Resour. Technol., **133**(4), p. 042901.
[5] Trevisan, F. E., and Prado, M. G., 2011, "Experimental Investigation of the Viscous Effect on Two-Phase Flow Patterns and Hydraulic Performance of Electrical Submersible Pumps," J. Can. Pet. Technol., **50**(4), pp. 1–8.
[6] Zhang, J., Cai, S., Li, Y., Zhu, H., and Zhang, Y., 2016, "Visualization Study of Gas-Liquid Two-Phase Flow Patterns Inside a Three-Stage Rotodynamic Multiphase Pump," Exp. Therm. Fluid Sci., **70**(1), pp. 125–138.
[7] Monte Verde, W., Biazussi, J. L., Sassim, N. A., and Bannwart, A. C., 2017, "Experimental Study of Gas-Liquid Two-Phase Flow Patterns Within Centrifugal Pumps Impellers," Exp. Therm. Fluid Sci., **85**(1), pp. 37–51.
[8] Cubas Cubas, J. M., 2017, "Experimental Study of Biphasic Flow Air-Water in a Radial Centrifugal Pump," Master's thesis, Federal University of Technology, Curitiba, Brazil.
[9] Mohammadi, M., and Sharp, K. V., 2013, "Experimental Techniques for Bubble Dynamics Analysis in Microchannels: A Review," ASME J. Fluids Eng., **135**(2), p. 021202.
[10] Minemura, K., and Murakami, M., 1980, "A Theoretical Study on Air Bubble Motion in a Centrifugal Pump Impeller," ASME J. Fluids Eng., **102**(4), pp. 446–453.
[11] Sabino, R. H. G., 2015, "Analysis of Dynamic of a Gas Bubble in a Centrifugal Pump," Master's thesis, Federal University of Technology, Curitiba, Brazil.
[12] Khalil, M., Kassab, S., Ismail, A., and Elazab, I., 2008, "Centrifugal Pump Performance Under Stable and Unstable Oil-Water Emulsions Flow," 12th International Water Technology Conference, Alexandria, Egypt, Mar. 27–30.
[13] Morales, R., Pereyra, E., Wang, S., and Shoham, O., 2013, "Droplet Formation Through Centrifugal Pumps for Oil-in-Water Dispersions," SPE J., **18**(1), pp. 172–178.
[14] Bulgarelli, N. A. V., Biazussi, J. L., Castro, M. S., Monte Verde, W., and Bannwart, A. C., 2017, "Experimental Study of Phase Inversion Phenomena in Electrical Submersible Pumps Under Oil-Water Flow," 36th International Conference on Ocean, Offshore and Arctic Engineering (OMAE), Trondheim, Norway, June 25–30.
[15] Perissinotto, R. M., Monte Verde, W., Biazussi, J. L., Castro, M. S., and Bannwart, A. C., 2017, "Visualization of Oil Droplets Within ESP Impellers," 36th International Conference on Ocean, Offshore and Arctic Engineering (OMAE), Trondheim, Norway, June 25–30.
[16] Sadhal, S. S., Ayyaswamy, P. S., and Chung, J. N., 1997, "Transport Phenomena With Drops and Bubbles," *Mechanical Engineering Series*, Springer, New York.
[17] White, F. M., 2011, *Fluid Mechanics*, 7th ed., McGraw-Hill, New York.
[18] Gülich, J. F., 2007, *Centrifugal Pumps*, Springer, Berlin.
[19] Pedersen, N., Larsen, P. S., and Jacobsen, C. B., 2003, "Flow in a Centrifugal Pump Impeller at Design and Off-Design Conditions—Part I: Particle Image Velocimetry (PIV) and Laser Doppler Velocimetry (LDV) Measurements," ASME J. Fluids Eng., **125**(1), pp. 61–72.
[20] Byskov, R. K., Jacobsen, C. B., and Pedersen, N., 2003, "Flow in a Centrifugal Pump Impeller at Design and Off-Design Conditions—Part II: Large Eddy Simulations," ASME J. Fluids Eng., **125**(1), pp. 73–83.